Quantum Superinductor with Tunable Non-Linearity: Supplementary Materials

M.T. Bell,[1] I.A. Sadovskyy,[1] L.B. Ioffe,[1] A.Yu. Kitaev,[2] and M.E. Gershenson[1]

[1] *Department of Physics and Astronomy, Rutgers University, Piscataway, NJ 08854, USA and*
[2] *Caltech, Institute for Quantum Information, Pasadena, CA 91125, USA*

I. EXPERIMENTAL DETAILS

A. Device fabrication

The superinductor, the lumped-element *LC* resonator, and the microstrip feedline line were fabricated within the same vacuum cycle using multi-angle electron-beam deposition of Al films through a nanoscale lift-off mask. To minimize the spread of the junction parameters, we have used the so-called "Manhattan-pattern" bi-layer lift-off mask formed by a 400-nm-thick e-beam resist (the top layer) and 50-nm-thick copolymer (the bottom layer). In this technique, the circuit is formed by aluminum strips of a well-controlled width intersecting at right angles (thus, the "streets" and "avenues"). After depositing the photoresist on an undoped Si substrate and exposing the pattern with e-beam lithography, the sample was placed in an ozone asher to remove any traces of the photoresist residue. This step is crucial for reducing the spread in junction parameters.

The substrate was then placed in an oil-free high-vacuum chamber with a base pressure of 5×10^{-9} mbar. The rotatable substrate holder is positioned at an angle of 45° with respect to the direction of e-gun deposition of Al. During the first Al deposition, the substrate was positioned such that the "streets" were orthogonal to the deposition direction. If the width of lines in the e-beam resist forming the "streets" is less than the mask thickness ($0.45\,\mu$m), no metal is deposited in the "streets" during this deposition, whereas the "avenues" are fully covered with Al. Alternatively, if the lines forming the "streets" are wider than $0.5\,\mu$m, both the "streets" and "avenues" are covered with metal in the first deposition. The lines narrower than $0.5\,\mu$m were used to form Josephson junctions, the wider lines were used for the fabrication of meander-shaped inductors. Without breaking vacuum, the surface of the bottom Al layer with a thickness of 20 nm was oxidized at ~ 100 mTorr of dry oxygen for 5 minutes.

After evacuating oxygen, the substrate holder was rotated by 90°, and the second 60-nm-thick Al film was deposited; this layer forms top electrodes of Josephson junctions, and increases the total thickness of the meander-shaped inductors and interdigitated capacitors. Finally, the sample was removed from the vacuum chamber and the lift-off mask was dissolved in the resist remover. The spread of the resistances for the nominally identical JJs with an area of $0.15 \times 0.15\,\mu$m^2 did not exceed 10%.

B. Measurement technique

The microwave response of the coupled superinductor and *LC* resonators was probed by measuring both the phase and amplitude of the microwaves traveling along a microstrip feedline coupled to the resonators. A simplified schematic of the microwave circuit is shown in Fig. S1. The cold attenuators and low-pass filters in the input microwave line prevented leakage of thermal radiation into the resonator. On the output line, two cryogenic Pamtech isolators (~ 18 dB isolation between 3 and 12 GHz) anchored to the mixing chamber were used to attenuate the ~ 5 K noise from the cryogenic amplifier.

The probe microwaves at frequency ω_1, generated by a microwave synthesizer (Anritsu MG3694B), were coupled to the cryostat input line through a 16 dB coupler. These microwaves, after passing the sample, were amplified by a cryogenic HEMT amplifier (Caltech CITCRYO 1-12, 35 dB gain between 1 and 12 GHz) and two 30 dB room-temperature amplifiers. The amplified signal was mixed by mixer M_1 with the local oscillator signal at frequency ω_r, generated by another synthesizer (Gigatronics 910). The intermediate-frequency signal $A(t) = A \sin(\Omega t + \phi_0) + A_N(t)$ (where $A_N(t)$ is the noise term) at $\Omega = (\omega_1 - \omega_r)/2\pi = 30$ MHz was digitized by a 1 GS/s digitizing card (AlazarTech ATS9870). The signal was digitally multiplied by $\sin(\Omega t)$ and $\cos(\Omega t)$ averaged over $\sim 10^6$ periods, and its amplitude A (proportional to the microwave amplitude $|S_{21}|$) and phase ϕ were extracted as $A = \langle [A(t) \sin(\Omega t)]^2 + [A(t) \cos(\Omega t)]^2 \rangle^{1/2}$ and $\phi = \arctan\{\langle [A(t) \sin(\Omega t)]^2 \rangle / \langle [A(t) \cos(\Omega t)]^2 \rangle\}$, respectively. The reference phase ϕ_0 (which randomly changes when both ω_1 and ω_2 are varied in measurements) was found using similar processing of the low-noise signal provided by mixer M_2 and digitized by the second channel of the ADC. This setup enables accurate measurements of small changes $\phi - \phi_0$ unaffected by the phase jitter between the two synthesizers. The low noise of this setup allowed us to perform measurements at a microwave excitation level of -133 dBm which corresponded to a sub-single-photon population of the tank circuit. In the second-tone measurements, the superinductor resonator was excited by the microwaves at frequency ω_2 propagating along the same microwave feedline that was used for the microwave transmission at ω_1.

II. THEORETICAL ANALYSIS

Here we explain in detail the nature of the large inductances of the Josephson ladders studied in this work,
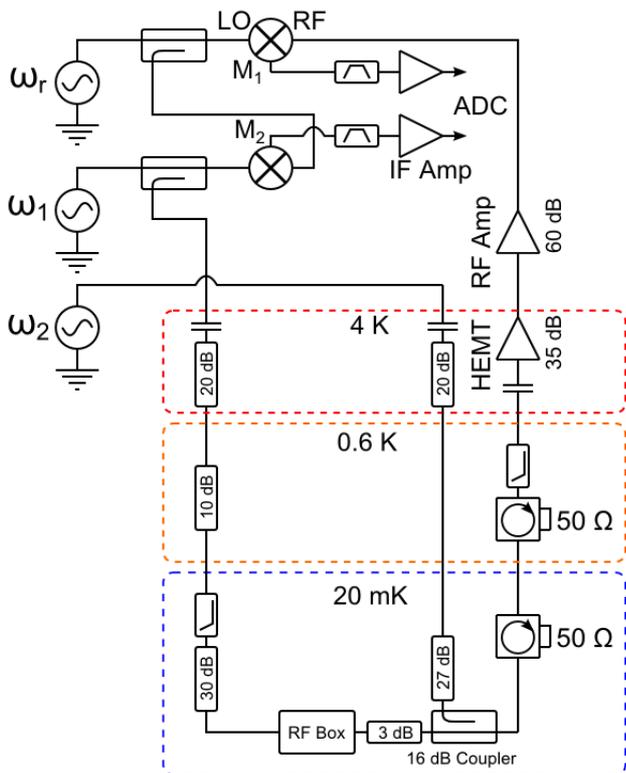
Figure 1: Simplified circuit diagram of the measurement setup. The microwaves at the probe frequency ω_1 are transmitted through the microstrip line coupled to the superinductor and LC resonators. The microwaves at ω_r, after mixing with the microwaves at ω_1, provided the reference phase ϕ_0. The signal at ω_1 is amplified, mixed down to an intermediate frequency $\omega_1 - \omega_r$ by mixer M_2, and digitized by a fast digitizer (ADC). The second channel of the ADC is used to digitize the signal from mixer M_2. The microwaves at the second-tone frequency ω_2 were coupled to the transmission line via a 16 dB coupler.

the role played by the field induced frustration and the numerical computations which results we compared with the data in the main text. We begin our discussion with the analysis of the classical (the Coulomb energy $E_C = 0$) model. We then discuss the computation that takes into account quantum fluctuations induced by a non-zero E_C.

A. Classical analysis

The main idea of the superinductor design becomes more transparent in the case of a fully frustrated ($\Phi = \Phi_0/2$) long ladder shown in Fig. S2(a). As we explain below, the fully frustrated regime is also very important experimentally because in this regime the quantum states of the ladder are less sensitive to the flux noise.

It is convenient to choose the gauge in which the magnetic field induces the phases $2\pi\Phi/\Phi_0$ on smaller junctions. Because at full frustration these phases are equal
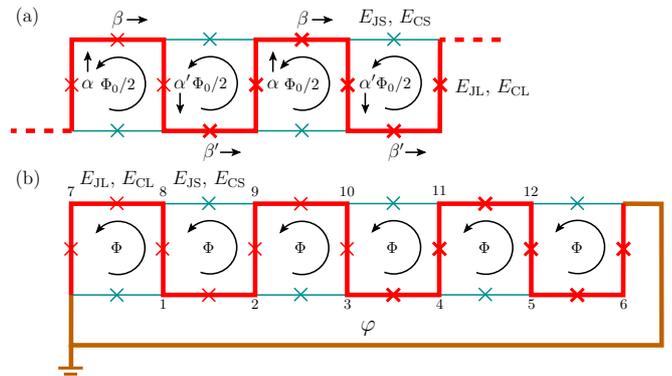

Figure 2: (a) A small portion of a long fully frustrated Josephson ladder. Large junctions with the Josephson energy E_{JL} and the Coulomb energy $E_{CL} \ll E_{JL}$ are shown in red thick lines; they form the ladder backbone. Small junctions with the Josephson energy E_{JS} and the Coulomb energy $E_{CS} \ll E_{JS}$ are shown in cyan thin lines. The frustration of each cell is controlled by the dimensionless parameter Φ/Φ_0. (b) Schematic diagram of a six cell ladder (device 1). The ends of the ladder are grounded: the phase difference across the ladder is φ.

to π, the shift of the ladder by one unit cell combined with its rotation about its axis transforms the ladder into itself, so the problem becomes translationally invariant. Furthermore, a large length of the ladder allows to neglect the boundary effects and focus on translationally invariant solutions.

Consider a small portion of the fully frustrated ladder shown in Fig. S2(a). The translational invariance implies that the solution is described by two phases across large junctions: α at the "vertical" junctions and β at the "horizontal" ones. The total phase across the whole ladder is $\varphi = N(\alpha + \beta)$, where N is the number of rungs. The energy per unit cell that contains two large and one small junctions is given by

$$E(\alpha, \beta) = -E_{JL}(\cos\alpha + \cos\beta) - E_{JS}\cos(\pi - 2\alpha - \beta). \quad (1)$$

The dependence $E(\alpha, \beta)$ is shown in Fig. S3(a). At $E_{JL} \gg E_{JS}$ the first term in Eq. (1) dominates and $E(\alpha, \beta)$ has a minimum at $(\alpha, \beta) = (0, 0)$. The expansion near this point gives

$$E^{(2)}(\alpha, \beta) = \frac{1}{2}\begin{bmatrix} \alpha & \beta \end{bmatrix}\begin{bmatrix} E_{JL} - 4E_{JS} & -2E_{JS} \\ -2E_{JS} & E_{JL} - E_{JS} \end{bmatrix}\begin{bmatrix} \alpha \\ \beta \end{bmatrix}, \quad (2)$$

which is a quadratic form with eigenvalues E_{JL} and $E_{JL} - 5E_{JS}$. The second eigenvalue changes sign as the ratio $r = E_{JL}/E_{JS}$ decreases, signaling the instability and appearance of a nontrivial ground state. The critical value of the ratio, $r_o = 5$, corresponds to the optimal working point, as explained below. At this point the function $E(\alpha, \beta)$ becomes flat along the eigenvector $(2, 1)$. We introduce new coordinates in the "flat" and "steep" directions: $\gamma = (2\alpha + \beta)/\sqrt{5}$, $\delta = (\alpha - 2\beta)/\sqrt{5}$. Figure S3(b)
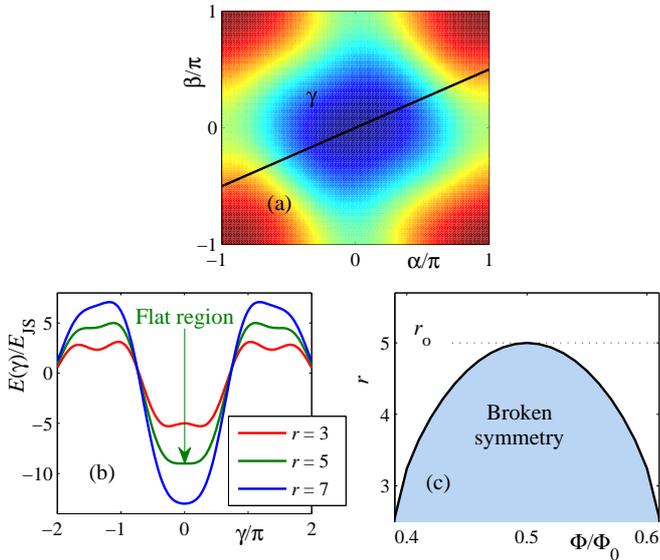
Figure 3: (a) Energy per elementary cell $E(\alpha, \beta)$ (1) as a function of α and β at the optimal point $r = r_o$. The black line corresponds to the flat direction parametrized by γ. (b) The dependence of energy in the flat direction for different values of r. (c) Phase diagram of the model in classical approximation in dimensionless variables $r = E_{JL}/E_{JS}$ and Φ/Φ_0. Quantum fluctuations discussed in section II B shift the transition line down but affect neither the long range order nor the phase transition.

shows the energy plotted along the flat direction. Neglecting the phase deviations in the steep direction, the total phase is related to γ by $\varphi = 3N/\sqrt{5}\gamma$.

At $r > r_o$ the ground state values of phases γ and φ, γ_0, and φ_0, are zero. Deviations of the total phase from $\varphi_0 = 0$ result in the quadratic increase of the energy

$$E^{(2)}(\varphi) = \frac{5}{18N}E_{JS}(r - r_o)\varphi^2.$$

At the optimal point ($r = r_o$) these deviations vanish, and the inductance, which is inversely proportial to $d^2E/d\varphi^2$, becomes infinite in the quadratic approxiamtion and is defined by the non-vanishing quartic term

$$E^{(4)}(\varphi) = \left.\frac{625 - 17r}{48600N^3}E_{JS}\varphi^4\right|_{r=r_o} = \frac{1}{90N^3}E_{JS}\varphi^4.$$

At smaller $r < r_o$ the ground state corresponds to a non-zero value of $|\gamma_0(r)| \propto \sqrt{r_o - r}$ that translates into a non-zero $\varphi_0 = \pm 3N\gamma_0/\sqrt{5}$. The appearance of a non-zero γ_0 is equivalent to a phase transition.

The translational invariance discussed above is violated away from full frustration. At arbitrary frustration, the ladder remains symmetric under the translation by two unit cells. Denoting the phases across the large junctions in the first cell by α, β and in the second cell by α', β' we

obtain the classical energy per two rungs

$$E(\Phi) = -E_{JL}\left[\cos\alpha + \cos\beta + \cos\alpha' + \cos\beta'\right]$$
$$-E_{JS}\left[\cos(\frac{2\pi\Phi}{\Phi_0} - \alpha_+ - \beta) + \cos(\frac{2\pi\Phi}{\Phi_0} + \alpha_+ + \beta')\right],$$
$$(3)$$

where $\alpha_+ = \alpha + \alpha'$. This energy does not change under the combined transformation $\alpha \to \alpha'$, $\beta \to \beta'$, and $\Phi \to -\Phi$, which correspond to the shift by one unit cell and simultaneous change in the sign of the magnetic field. The total phase difference along the ladder $\varphi = N(\alpha_+ + \beta_+)/2$ is invariant under this transformation. Time inversion invariance implies that the ground state energy does not change under the simultaneous change in sign in both Φ and φ, the symmetry under the combined transformation implies that the ground state energy is an even function of φ at any field. This conclusion is based only on the symmetry of the problem and thus remains valid when quantum fluctuations are taken into accound (see section II B).

The energy (1) is minimal at $\alpha_- = \alpha' - \alpha = 0$ and $\beta_- = (\beta' - \beta)/2 \neq 0$ that has to be determined from the minimization of (3). The minimum in α_-, β_- is always steep, so fluctuations in this direction can be neglected. In this approximation the general expression for the energy (3) is reduced to the form (1) with the effective

$$E_{JS}^{(eff)} = E_{JS}\cos(2\pi x + \beta_-),$$

where $x = \Phi/\Phi_0 - 1/2$.

At $r > r_o$ the ratio $E_{JL}/E_{JS}^{(eff)}$ that controls the instability is large: $E_{JL}/E_{JS}^{(eff)} > r > r_o$, so the ground state corresponds to zero phases. At $r < r_o$ the instability occurs at non-zero x_c, defined by $E_{JL}/E_{JS}^{(eff)}(x_c) = r_o$ [see Fig. S3(c)]. At the point of instability we can determine the value of β_- assuming that $\alpha_+ = \beta_+ = 0$, we get

$$\beta_-(x) = \arctan\left[\frac{\sin(2\pi x)}{r - \cos(2\pi x)}\right]. \quad (4)$$

The effective reduction of E_{JS} implies that at $r > r_o$ the transition from the single minimum at $\gamma = 0$ to double minimum at $\pm\gamma_0$ occurs as a function of the field at x_c where

$$\cos[2\pi x_c + \beta_-(x_c)] = \frac{r}{r_o}. \quad (5)$$

The transition line defined by Eqs. (4) and (5) separates a symmetry-broken (ordered) phase from the phase with unbroken symmetry. We show the phase diagram obtained by the numerical solution of these equations in Fig. S3(c). The equation for the instability can be solved analytically for $r_o - r \ll r_o$ (i.e. $x \ll 1$):

$$x_c = \frac{r}{2\pi(r + 1)}\arccos\left(\frac{r}{r_o}\right).$$

At the critical flux $\Phi_c = (1/2 \pm x_c)\,\Phi_0$ the quadratic part of the energy vanishes which implies infinite inductance. Thus, the system can be tuned to the infinite inductance either by realizing $r = r_o$ at full frustration, or by approaching Φ_c at $r < r_o$.

In the absence of noises and disorder, these two methods of realization of the infinite inductance (and the phase transition) are equivalent. However, the real systems are subject to flux noise. Because the energy of the ground state is quadratic in flux deviations $\delta\Phi$, the effect of the flux noise on the system is minimized if the infinite inductance is realized at full frustration, or close to it. Thus, the optimal working point corresponds to the ratio $E_{\mathrm{JL}}/E_{\mathrm{JS}} = r_o$.

The finite length of the ladder brings in two effects associated with the boundaries. First, this may violate the symmetry which resulted in $E(\varphi) = E(-\varphi)$ for all frustrations; this is crucial for the realization of infinite inductance at $\Phi_c \neq \Phi_0/2$. However, this effect is absent for the odd number of rungs (this was the reason for selecting the even number of unit cells in the studied ladders). In this case the ladder remains symmetric under the rotation by π about its center. The rotation does not change the magnetic fluxes but changes $\varphi \rightarrow -\varphi$, so in this case the function $E(\varphi)$ remains even for all fluxes and r. Second, the finite-size effects decrease the value of the critical r at which the instability occurs at full frustration. To compute them for finite ladders we numerically computed the energy $E(\varphi)$ for the ladders containing from 2 to 7 rungs. The dependences of the inductance $L_{\mathrm{K}}(\Phi, r) = \left(d^2 E/d\varphi^2\right)^{-1}\big|_{\varphi=\varphi_0}$ for different ladder lengths are shown in Fig. S4. The value of φ_0 is defined by the minimum of the ground state energy $E(\varphi)$ as a function of the phase φ. The inductance increases with frustration and diverges at full frustration $\Phi = \Phi_0/2$ for $r = r_o$. For the ladders with six unit cells, the finite size effects lead to a small decrease of the optimal value to $r_o = 4.8$.

B. Quantum analysis

Non-zero (but small) charging energies result in quantum fluctuations of the phase of individual islands, θ_i. These fluctuations have three effects. First, they might result in a phase slip in which the phase difference $\eta_{ij} = \theta_i - \theta_j$ between two islands connected by a large Josephson junction changes by 2π due to a quantum tunneling process. Second, they may result in renormalization of the effective energy in the flat direction discussed in section II A and the shift of the phase boundary in Fig. S3(c). Finally, they may have a very large effect on the properties of long ladders close to the transition point at which critical fluctuations are expected to become important.

In the absence of frustration the amplitude of a phase slip across a single large junction, $E_{\mathrm{ph}} \approx$
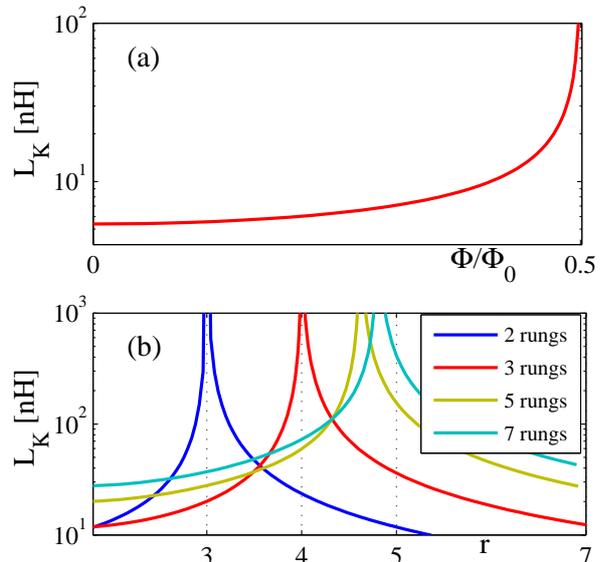

Figure 4: (a) Inductance as a function of frustration (external magnetic field) in the classical approximation for a three-rung ladder at $r = r_o$. (b) The inductance as a function of the ratio $r = E_{\mathrm{JL}}/E_{\mathrm{JS}}$ for ladder with 2, 3, 5, and 7 rungs. Optimal ratios r_o: 3 for 2 rungs, 4 for 3 rungs, 4.61 for 5 rungs, and 4.80 for 7 rungs.

$3.8 E_{\mathrm{CL}}^{1/4} E_{\mathrm{JL}}^{3/4} \exp(-\sqrt{8 E_{\mathrm{JL}}/E_{\mathrm{CL}}})$, is exponentially small for the experimental values of $E_{\mathrm{JL}}/E_{\mathrm{CL}} \approx 100$. The frustration decreases the tunnel barrier resulting in larger phase slip amplitudes. However, this effect is numerically small. Namely, the dominant transitions correspond to the process in which the phase β changes between 0 and 2π [see Fig. S3(a)], the action for this process is $S \approx 2.5\sqrt{E_{\mathrm{JL}}/E_{\mathrm{CL}}}$. Thus, the phase slip amplitudes remain negligible for the ladders with experimental parameters.

Small quantum fluctuations of the phase differences smear the classical potential. As a result the large inductance and the phase transition are realized at a smaller value of r_o. To estimate this effect we have diagonalized numerically the Hamiltonian describing small ladders. This diagonalization is convenient to perform in the charge basis in which the general Hamiltonian of the Josephson circuit acquires the form

$$\hat{H} = -\sum_{\langle i,j\rangle} \frac{J_{ij}}{2}\left(e^{-iA_{ij}}\mathbf{b}_i^+\mathbf{b}_j^- + \mathrm{H.c.}\right)$$
$$+ (2e)^2 \sum_{i,j} (C^{-1})_{ij}(n_i + q_i)(n_j + q_j), \qquad (6)$$

where matrix J_{ij} describes Josephson couplings between islands and C_{ij} is the capacitance matrix of the system. For large junctions $J_{i,i+1} = E_{\mathrm{JL}}$, $C_{i,i+1} = C_{\mathrm{L}}$, and $E_{\mathrm{CL}} = e^2/2C_{\mathrm{L}}$; for small junctions $J_{i,i+3} = E_{\mathrm{JS}}$, $C_{i,i+3} = C_{\mathrm{S}}$, and $E_{\mathrm{CS}} = e^2/2C_{\mathrm{S}}$. The operators $\mathbf{b}^{\pm}$ increase (decrease) the number of Cooper pairs on each
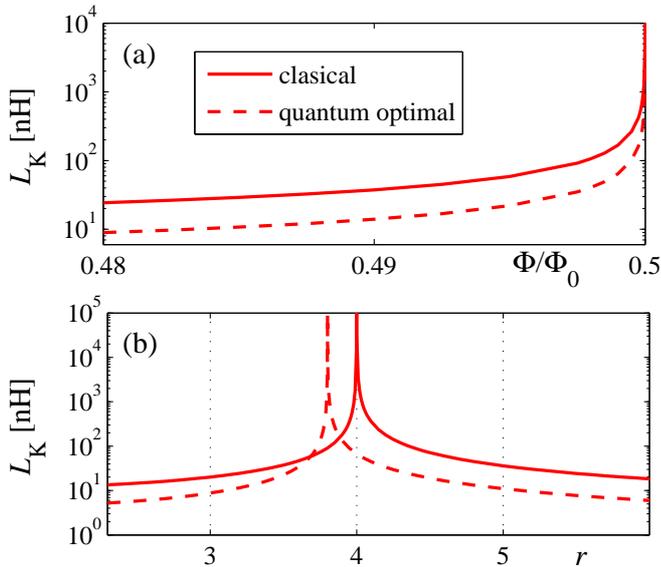
Figure 5: Solid lines in panels (a) and (b) show the inductance computed in the classical approximation for a three-rung ladder as a function of frustration at $r = r_o$ (a) and as a function of r for $\Phi = \Phi_0/2$ (b). Dashed lines show the results of the full quantum computation for the same ladder. Quantum fluctuations shift position of the optimal point from its classical value ($r_o = 4$) to $r_o \approx 3.8$. Dashed line in panel (a) shows the result of the full quantum computation at $r = r_o$ which takes into account the shift of r_o due to quantum fluctuations.

island: $\mathbf{b}_i^{\pm} = |n_i \pm 1\rangle_i \langle n_i|$. The junction matrix J_{ij} is symmetric and its diagonal terms are zeros. The capacitance matrix C_{ij} is positively defined with positive diagonal elements C_{ii} and negative off-diagonal elements C_{ij}, $i \neq j$, so that its inverse $(C^{-1})_{ij}$ is positively defined and its elements are all positive. The phases A_{ij} are induced by the magnetic field, the sum of A's over a closed loop l of n Josephson junctions corresponds to the flux Φ_l penetrating this loop.

For the numerical diagonalization we had to limit the number of charging states, n_q at each island. For the parameters similar to the experimental ones it is sufficient to keep $n_q = 12$ to get the results with better than 1% accuracy. The effect of the quantum fluctuations on the inductance of a three rung chain with $E_{JL}/E_{CL} = 40$ is shown in Fig. S5. We observe that quantum fluctuations reduce r_o by $\delta r \approx 0.2$ down from its classical value, but the behavior of the inductance as a function of the frustration remains essentially the same. The importance of quantum fluctuations increases with the ladder length, so this shift becomes $\delta r \approx 0.5$ for the ladders with six unit cells.

The inductance L can be calculated as the inverse curvature of the ground state energy $E(\varphi)$. Alternatively, it can be defined as $L = 1/\omega_{01}^2 C$ for a superinductor shunted by a capacitor C. Here the frequency ω_{01} is the excitation frequency of the superinductor resonator $\omega_{01} = E_1 - E_0$. In the limit of a large capacitance C

both methods give the same result (for a linear circuit, the results of both methods are identical for any C).

For the detailed comparison with the data for device 1 we have diagonalized the Hamiltonian of the ladder connected to a large capacitor. In this Hamiltonian we used the values of the charging energy of small junctions and their Josephson energy extracted from the independent measurements of the Cooper pair transistors containing nominally identical junctions with $E_{CS} = 0.46$ K and $E_{JS} = 3.2$ K. The value of the charging energy of the large junction that was calculated from the ratio of the areas of small and large junctions: $E_{CL} = 0.15$ K. We used the designed value of the large capacitance $C_K = 18$ fF. We then diagonalized the Hamiltonian of the ladders containing up to six rungs, determined the excitation frequency of the superinductor resonator, $\omega_{01}(\Phi) \equiv E_1 - E_0$, and extrapolated the result to 7 rungs that cannot be computed directly due to an enormous size of the Hilbert space. For the experimental values of the charging energies r_o is shifted down to approximately 4.1. The 7-rung devices studied in this work (e.g. device 1) are characterized by the ratios r that are significantly above r_o, so the extrapolation to seven rungs works reasonably well. We found that in this parameter range the form of the dependence $\omega_{01}(\Phi)$ in the interval $0.4 < \Phi/\Phi_0 < 0.5$ is very similar for different r, whilst the absolute values of $\omega_{01}(0.4\Phi_0)$ and $\omega_{01}(0.5\Phi)$ change dramatically as a function of r. This dependence is plotted in Fig. 3(a) of the main text. Fitting the ratio $\omega_{01}(0.4\Phi_0)/\omega_{01}(0.5\Phi_0)$ to experimental values for device 1 gives for the ratio $r = 4.5$ that is close to the designed value of 4.0.

The energy of the first excited states of longer device 2 was obtained in a two step procedure. In the first step we used exact diagonalization to find the energy functional of small quantum ladders (with 3-5 rungs) forming the loop penetrated by flux $\Phi = \Phi_0/2$ and fit it to the general form expected in vicinity of the optimal point:

$$E(\varphi) = \frac{B_q(r)}{N} E_{JS} \varphi^2 + \frac{C_q(r)}{N^3} E_{JS} \varphi^4. \tag{7}$$

Here $B_q(r)$ and $C_q(r)$ are numerical coefficients that differ somewhat from their classical values, B_{cl} and C_{cl}. Comparison of the results of the computation with classical result shows that the main effect of quantum computation is a shift of the critical value of r (see Fig. 6), $B_q(r) \approx B_{cl}(r + \delta r)$ with $\delta r \approx 0.45$ and a modest renormalization of $C_q(r) \approx 0.7 C_{cl}(r = r_o)$ that can be approximated by the constant in the relevant regime.

The procedure outlined above allowed us to determine the renormalization of the classical energy by short scale quantum fluctuations. In the second step we used Eq. (7) to compute the potential energy of the long ladder of device 2. Solving finally the quantum problem of the phase fluctuations across the whole ladder characterized by the Hamiltonian
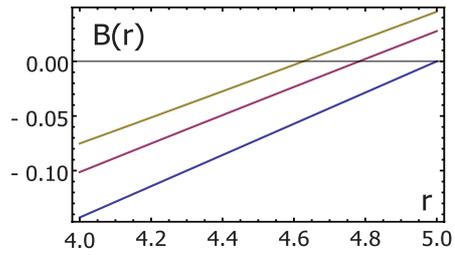
$$H = E(\varphi) + 4E_C q^2$$

Figure 6: Classical and quantum $B(r)$. From right to left: the results of classical computation and from the full diagonalization of Hamiltonians for three and four rungs ladders.

we find the low energy excitations of the device. The results are shown in Fig. 3(b) of the main text.